

Research article

Weifang Lu*, Mizuki Terazawa, Dong-Pyo Han, Naoki Sone, Nanami Goto, Kazuyoshi Iida, Hedeki Murakami, Motoaki Iwaya, Tetsuya Tekeuchi, Satoshi Kamiyama and Isamu Akasaki

Structural and optical impacts of AlGaN undershells on coaxial GaInN/GaN multiple-quantum-shells nanowires

<https://doi.org/10.1515/nanoph-2019-0328>

Received August 25, 2019; revised October 18, 2019; accepted November 11, 2019

Abstract: The superior crystalline quality of coaxial GaInN/GaN multiple-quantum shell (MQS) nanowires (NWs) was demonstrated by employing an AlGaN undershell during metal-organic chemical vapor deposition. Scanning transmission electron microscopy (STEM) results reveal that the NW structure consists of distinct GaInN/GaN regions on different positions of the NWs and the cores were dislocation-free. High-resolution atomic contrast STEM images verified the importance of AlGaN undershells in trapping the point defects diffused from *n*-core to MQSs (*m*-planes), as well as the improvement of the grown crystal quality on the apex region (*c*-planes). Time-integrated and time-resolved photoluminescence (PL) measurements were performed to clarify the mechanism of the emission within the coaxial GaInN/GaN MQS NWs. The improved internal quantum efficiency in the NW sample was attributed to the unique AlGaN undershell, which was able to

suppress the point defects diffusion and reduce the dislocation densities on *c*-planes. Carrier lifetimes of 2.19 ns and 8.44 ns were derived from time-resolved PL decay curves for NW samples without and with the AlGaN undershell, respectively. Hence, the use of an AlGaN undershell exhibits promising improvement of optical properties for NW-based white and micro light-emitting diodes.

Keywords: AlGaN undershell; point defect diffusion; internal quantum efficiency (IQE); nanowires (NWs); GaInN/GaN MQS.

1 Introduction

Improving the crystalline quality of GaN-based semiconductors is essential for the applications in solid-state lighting equipment and display systems [1, 2]. However, the performance of conventional light-emitting diodes (LEDs) suffers from high dislocation density and efficiency droop induced by the quantum-confined Stark effect (QCSE) [3, 4]. Over the past decade, GaN-based nanowires (NWs) have received significant attention as a prime candidate for future high-performance nanoscale-optoelectronic devices, such as white LEDs, nanoscale lasers, and micro-LEDs [5–12]. GaInN/GaN coaxial NW structures have a large surface-to-volume ratio and possess intriguing advantages in comparison to their thin-film/bulk counterparts: (i) significantly reduced threading dislocations, (ii) improvement of light extraction efficiency, (iii) absence of the QCSE in nonpolar *m*-planes of the NWs, and (iv) large active regions with a core-shell geometry on *m*- and *r*-planes [3, 13, 14]. In addition, the incorporation of indium in GaInN/GaN multiple-quantum-shells (MQSs) can be tuned with the NW diameter, providing the possibility to achieve monolithically integrated white light emission [15, 16].

To achieve high-performance NW-based devices, one obstacle to overcome is the performance degradation caused by point defects like vacancies and impurities

***Corresponding author: Weifang Lu**, Department of Materials Science and Engineering, Meijo University, 1-501 Shiogamaguchi, Tenpaku-ku, Nagoya, 468-8502, Japan, e-mail: nianyulu@outlook.com, weif@meijo-u.ac.jp. <https://orcid.org/0000-0001-6214-4024>

Mizuki Terazawa, Dong-Pyo Han, Nanami Goto, Hedeki Murakami, Motoaki Iwaya, Tetsuya Tekeuchi and Satoshi Kamiyama:

Department of Materials Science and Engineering, Meijo University, 1-501 Shiogamaguchi, Tenpaku-ku, Nagoya, 468-8502, Japan

Naoki Sone: Department of Materials Science and Engineering, Meijo University, 1-501 Shiogamaguchi, Tenpaku-ku, Nagoya, 468-8502, Japan; and Koito Manufacturing Co., Ltd, Research and Development Department, Tokyo 108-8711, Japan

Kazuyoshi Iida: Department of Materials Science and Engineering, Meijo University, 1-501 Shiogamaguchi, Tenpaku-ku, Nagoya, 468-8502, Japan; and Toyota Gosei Co., Ltd, Optical Electronics Department, Aichi 452-8564, Japan

Isamu Akasaki: Department of Materials Science and Engineering, Meijo University, 1-501 Shiogamaguchi, Tenpaku-ku, Nagoya, 468-8502, Japan; and Akasaki Research Center, Nagoya University, Furo-cho, Chikusa-ku, Nagoya 460-8601, Japan

[17, 18]. The point defects are easily segregated on the GaN surface during growth [19] and transferred into the GaInN/GaN active region, due to the lower formation energy with the increased incorporation of In [20, 21]. An independent phenomenon with dislocation density was observed in GaInN/GaN LEDs under high-current recombination terms [22], while the point defects mainly contributed to the nonradiative recombination process in the current density range of 10^{-2} – 10 A/cm² [23]. To date, most of the work reported on GaN-based NWs has focused on the growth mechanism and the optically pumped and electrically injected properties [7, 24–26]. However, less emphasis has been placed on the elimination/suppression of point defects diffusion in GaN-based NWs. To suppress the diffusion of point defects, alternative approaches such as GaInN underlayers and GaN/GaInN superlattice structures have been implemented to increase the In incorporation and improve the crystalline quality of NWs [27, 28]. In addition, A. Armstrong et al. have identified surface deep-level defects and an effective passivation mechanism of an AlGaIn shell on GaN NWs [29]. Fundamentally, the AlGaIn shell is likely to reduce the point defects on the surface of GaN core NWs due to lower surface mobility of Al, as well as a lower formation energy of vacancies in the AlGaIn layer than that in GaN core NWs [30–33]. For this reason, it is necessary to conduct a detailed investigation to gain insight into the trapping effect of point defects by the AlGaIn undershell in terms of its structural and optical impacts on coaxial GaInN/GaN MQS NWs.

In this study, we present a systematic study of the structural and optical properties of the coaxial GaInN/GaN MQSs NWs. The atomic resolution structural features of NWs with and without the AlGaIn undershell were characterized by scanning transmission electron microscopy (STEM). To better understand the effects of the AlGaIn undershell on the optical performance, temperature- and power dependent-photoluminescence (PL) spectra measurements were carried out on the coaxial GaInN/GaN NWs, where an intense emission from GaInN/GaN MQSs was observed. Band edge luminescence associated with GaN, along with broad point defect-related yellow luminescence in core NWs, has been observed. By introducing an AlGaIn shell underneath GaInN/GaN MQS, the yellowish luminescence from the core-GaN has been suppressed, while the emission intensity of MQS prominently increased. To assess the emission features, time-resolved PL was measured for establishing a direct correlation between structural and other emission properties. The role of the AlGaIn shell was deduced as a point defects trapping layer, resulting in reduction of non-radiative recombination centers. Such an investigation can shed some light on the effects

of the AlGaIn undershell on the quality improvement of GaInN/GaN multiple-quantum-shell NWs.

2 Experimental growth and characterization methods

A commercial GaN/sapphire substrate (Suchou Nanowin Science and Technology Co., Ltd, Suzhou, Jiangsu, China) was used as the basal template for NW array growth. A 30 nm thick SiO₂ layer was deposited on the substrate as a growth mask by using a radiofrequency magnetron sputtering system (CFS-4EP, Shibaura Mechatronics Co., Yokohama, Kanagawa, Japan). Subsequently, nanoimprint lithography (TEX-01, KYODO INTERNATIONAL INC., Kawazaki, Kanagawa, Japan) and dry etching were applied to open circular holes of 320 nm and 1200 nm in diameter and pitch distance, respectively. After preparing the aperture patterns on the GaN/sapphire template, a horizontal metal-organic chemical vapor deposition (MOCVD) system equipped with a 2-in susceptor (SR 2000, TAIYO NIPPON SANSO Co., Shinagawa-ku, Tokyo, Japan) was employed to carry out the growth process for core-shell NWs. The coaxially aligned n-GaN core, AlGaIn undershell, and GaInN/GaN MQS were sequentially grown. Specifically, the n-type GaN core NWs were synthesized on the template using trimethylgallium (TMG) and ammonia (NH₃) as precursors under continuous-flow mode. The growth temperature and pressure for core NWs was maintained at 1135°C and 90 kPa, respectively, where the flow rate ratio of NH₃ (100 sccm)/TMG (50 sccm) was fixed at 20. The Si doping was provided by a SiH₄ precursor with a flow rate of 1.25 sccm with pure hydrogen (H₂) as the carrier gas. Subsequently, a conformal AlGaIn undershell with 3% Al composition was coaxially grown on the core NWs at 840°C for 10.6 min. The flow rate of triethylgallium (TEG), NH₃, and trimethylaluminum were kept at 6000 sccm, 250 sccm, and 4 sccm, respectively. For the GaInN/GaN MQS structures, trimethylindium (350 sccm), TEG (30 sccm), and NH₃ (6000 sccm) were used as the precursors for quantum-well and barrier growth under ambient nitrogen. During the growth of five pairs of GaInN-well and GaN-barrier, the temperature was maintained at 740°C. For comparative studies, four NW samples a, b, c, and d were prepared, and the detailed information are listed in Table 1.

The surface morphology of the NW samples was characterized using a scanning electron microscopy (SEM) system (SU70, Hitachi High-Technologies Co., Minato City, Tokyo, Japan) operated at an acceleration voltage of 3 kV. The structural properties and crystalline quality along the

Table 1: MOCVD grown NW samples and characterizations.

Samples	NW structures	Structural characterization	Optical characterization	
			System	Excitation wavelength
a	n-core	SEM	Macro-PL	325 nm
b	n-core/ <u>MQS</u>	SEM + STEM	Macro-PL + Micro-PL	405 nm
c	n-core/AlGaIn	SEM	Macro-PL	325 nm
d	n-core/AlGaIn/ <u>MQS</u>	SEM + STEM	Macro-PL + Micro-PL	405 nm

NW of samples b and d were assessed by STEM. To characterize the cross-sectional structures, lamella across a single NW was prepared in a focused ion beam (FIB) dual beam system (FEI Helios NanoLab 450, Thermo Fisher Scientific, Waltham, MA, USA). A 150 nm thick protective layer of carbon and several dozens of nanometers of platinum (Pt) were deposited onto the preselected area of the NWs. Afterwards, several micrometers of carbon was deposited on the NWs using FIB to protect the surface of NWs from the FIB-induced damage during the milling process. An electron-transparent thin lamella can be obtained utilizing focused Ga ion sputtering operated at an accelerating voltage of 30 kV, and then followed by a cleaning process by a 2 kV Ga ion beam. The high-resolution measurements were carried out using a Hitachi HD2700 STEM system (Hitachi High Technologies Cor., Minato City, Tokyo, Japan) under an acceleration voltage of 200 kV and a nominal probe size around 0.1 nm. The STEM images were formed by electrons transmitted through the lamella, which scattered to higher angles, and then subsequently acquired using a high-angle annular dark-field (HAADF or Z-contrast) detector.

To analyze the emission properties, two different protocols were carried out for PL measurements, as illustrated in Figure 1A and B. Regarding the macro-PL setup,

the excitation source was a 325-nm He-Cd laser (IK Series, KIMMON KOHA Co. Ltd., Itabashi City, Tokyo, Japan) or 405-nm laser diode (NEOARK Corp., Hachioji, Tokyo, Japan), where the power densities were 0.71 mW/mm² and 4.87 mW/mm², respectively. The laser spot size in the macro-PL setup is approximately 1 mm in diameter, at an incident angle of 45°, and thus approximately 750 NWs can be measured. The emission signal was collected perpendicularly from the samples by a fiber spectrometer (USB4000, Ocean Optics Inc., Largo, FL, USA) through a fiber collimator. The PL measurements for samples b and d were conducted using a micro-PL setup with a 405-nm excitation laser (Cube Laser, CUBE 405-100C, Coherent Inc., Santa Clara, CA, USA). Both the excitation light and detection optical spectrometer (Fiber-optic Spectrometer, AvaSpec-ULS2048, Avantes, Apeldoorn, the Netherlands) are fiber-coupled to an optical microscope (Olympus Co., Shinjuku, Tokyo, Japan) and in parallel to the NW growth direction. The diameter of the laser spot focused on the NWs was 100 μm through a 20× objective lens, so several dozens of NWs (75 NWs) can be homogeneously excited. To exclude the effects of the excitation peak on the PL, the collected emission signal from NW samples was filtered through a low-pass filter with a cutoff wavelength

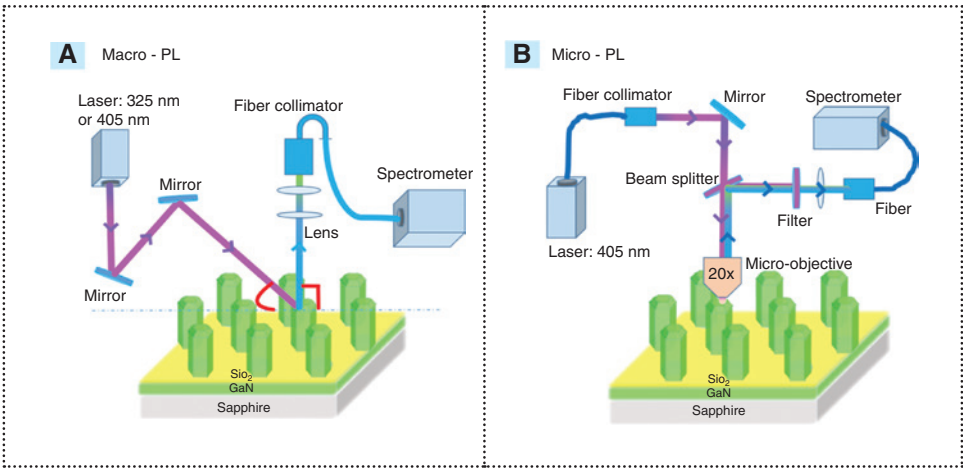


Figure 1: The schematic diagram of PL setup for NW samples. (A) Macro-PL setup for NW samples using 325 nm and 405 nm laser diodes, where the beam size is 1 mm in diameter and the incident angle is 45°. (B) Micro-PL setup for NW samples with 20× objective, while the NWs are excited and detected vertically in the confocal system with a spot size of 100 μm.

at 420 nm. The low temperature PL measurement for samples b and d was performed at 12 K, where the temperature was controlled using a closed cycle cryostat system (CS202-DMX-1AL, Advanced Research System, Macungie, PA, USA). Power-dependent PL measurements were carried out for samples b and d at room temperature using the same setup. Time-resolved PL spectra of samples b and d were measured at room temperature utilizing a picosecond pulsed laser system (C4780, Hamamatsu, Hamamatsu City, Shizuoka, Japan) coupled with a microscope. The picosecond-pulsed diode laser was controlled by a laser diode head (PLP-10 C10196, Hamamatsu) with a focusing lens (A10089, Hamamatsu, Hamamatsu City, Shizuoka, Japan). The excitation wavelength of the laser was 405 nm with a repetition rate of 10 MHz and pulse duration of ~ 70 ps. The emission light was filtered by a long pass filter of 410 nm. The signal was acquired by a synchroscan streak camera system (C4334, Hamamatsu, Hamamatsu City, Shizuoka, Japan) with a temporal resolution of 40 ps.

3 Results and discussion

After growth, the surface morphology of the four NW samples was evaluated by SEM, as illustrated in Figure 2. The NWs were grown perpendicularly to the polar c -plane

and exhibited six non-polar sidewalls (m -planes). The m -plane surfaces were exposed for subsequent growth of the AlGaIn undershell and GaInN/GaN MQS. As a reference sample, core NWs with a diameter of 380 nm and a height of 1.3 μm are depicted in Figure 2 (A_i) and (A_{ii}). Figure 2B displays the shape of the n-core + GaInN/GaN MQSs NWs. Some flakes are observed at the hexagonal corners of the NWs, which may be In-rich droplets. By employing an AlGaIn undershell, the diameter of sample d is larger than that of sample b, as shown in Figure 2 (D_i). After growing the coaxial AlGaIn undershell or/and GaInN/GaN MQSs, the as-grown NW samples are featured with a uniform shape exposing the c -, r -, and m -planes. In Figure 2 (C_i) and (D_i), a few crystals are observed on the SiO_2 mask surface in samples c and d, due to the low growth temperature and higher sticking coefficient of Al atoms during AlGaIn undershell growth [30]. At the top area of NWs in sample d, the diameter is larger than that of the bottom part. Distinctly different from the morphology of sample b, NWs in sample d exhibit a larger diameter and a smoother apex (without droplets) [Figure 2 (B_{ii}) and (D_{ii})]. Figure 2 (A_{iii})–(D_{iii}) depict the high resolution SEM images of the apex portion of the NWs, exhibiting that the formed r -plane during AlGaIn growth eliminated the formation of voids in the c -plane of the NWs.

In general, the emission wavelengths are related to the In incorporation and quantum well thickness at different

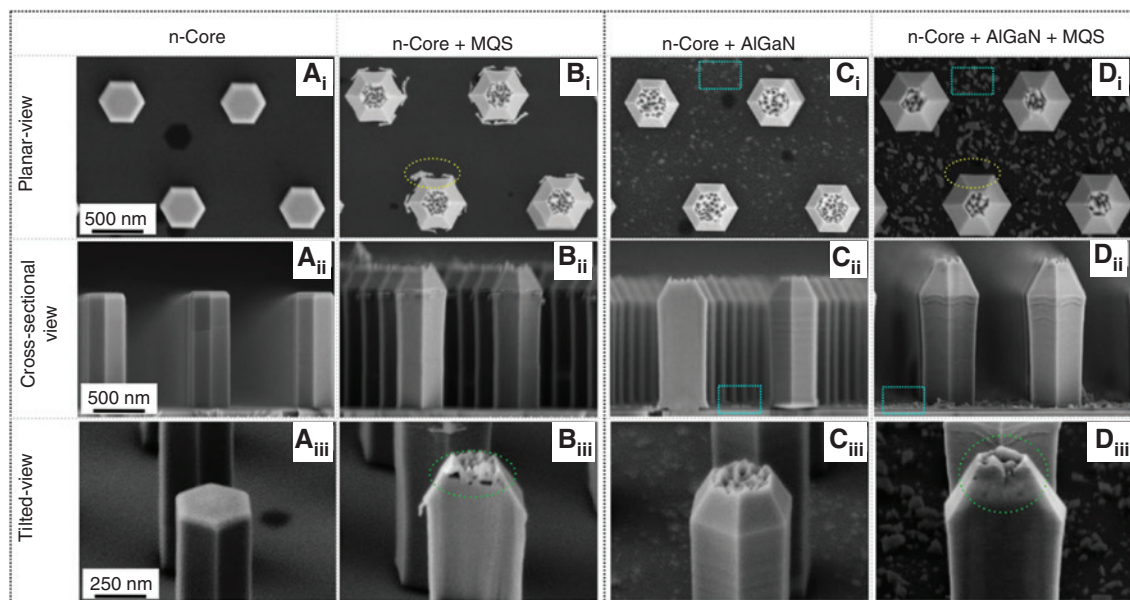


Figure 2: Planar and cross-sectional view SEM images of the NW samples a, b, c, and d, respectively, where the AlGaIn undershell were grown for 10.6 min at 840°C.

The differences between the samples are marked with dashed boxes. (A_i – A_{iii}) The SEM images of sample a with n-core structures. (B_i – B_{iii}) The SEM morphology of the NWs grown with MQS structures in sample b. The NWs contain In-rich droplets on the apex part. (C_i – C_{iii}) The SEM images of NW sample c, which covered with an AlGaIn shell. A few AlGaIn particles are observed on the SiO_2 mask layer. (D_i – D_{iii}) The planar and cross-sectional view SEM images of the MQS NW sample d. The formation of In-rich droplets and voids on the apex was suppressed.

facets. To analyze the insightful structure features of NWs, transmission electron microscopy measurements were carried out for samples b and d. The lamella was prepared along the growth direction $\langle 0001 \rangle$. The typical HAADF-STEM images of an individual NW in samples b and d are shown in Figure 3A and B. It is confirmed that the relatively uniform NW structures were grown by continuous flow mode MOCVD. The extended dislocations are hardly observed inside the n-core, indicating a superior crystalline quality. The absence of dislocation is an important advantage in the NW samples for high-performance NW-based devices. The presence of the GaInN/GaN MQS region grown on the sidewall of the n-core is clearly identified. In the HAADF-STEM images, the contrast is sensitive to the atomic number of the materials, as a smaller atomic number typically gives less elastically scattered electrons [34]. Hence, the brighter areas correspond to the GaInN wells, because the In is a heavier element than Ga and therefore scatters more electrons to the HAADF detector. The high resolution STEM images of different parts of the MQS NW are shown in Figure 3 (A_i)–(A_{iii}), which confirm the high crystalline quality. Five pairs of GaN barrier and GaInN well structures on NWs are visible as regular brighter/darker intervals on the sidewall of the NW. The thicknesses of the barrier and well are likewise

clearly distinguishable: 4.0 nm/1.9 nm, 7.5 nm/3.9 nm, and 4.2 nm/3.0 nm on the *r*- and *m*-planes of the top and middle part of the NWs, respectively. The MQS grown at the junction between the *r*- and *m*-planes are slightly thicker due to the migration of adatoms from the *r*-planes to *m*-planes. The In incorporation in this region is also expected to be rich, in accordance with observed droplets in Figure 2B. As in the case of sample d, the growth rate of the barrier and well on the *m*-plane decreased, owing to the increased diameter of NW with AlGaIn undershell under the same flow rates of precursors as for sample b. Hence, the total volume of each well or barrier on *m*-planes is expected to be the same in samples b and d. The formation of In-rich droplets was eliminated at the junction region between *r*- and *m*-planes, as shown in Figure 3 (B_{ii}). In comparison with the dimensions of the n-core in sample b, the thickness of AlGaIn undershell is estimated to be ~58 nm.

The top area of NWs is a critical part in fabricating NW-based LEDs with high performance, since the low crystalline quality might provide additional leakage paths through dislocations or point defects. The apex part of a NW in sample b exhibited a pyramidal shape with rough morphology as shown in Figure 4A, which may be due to the high impinging rate of precursors during the growth of GaInN/GaN MQSs on *c*-planes. Thus, the In adatoms were

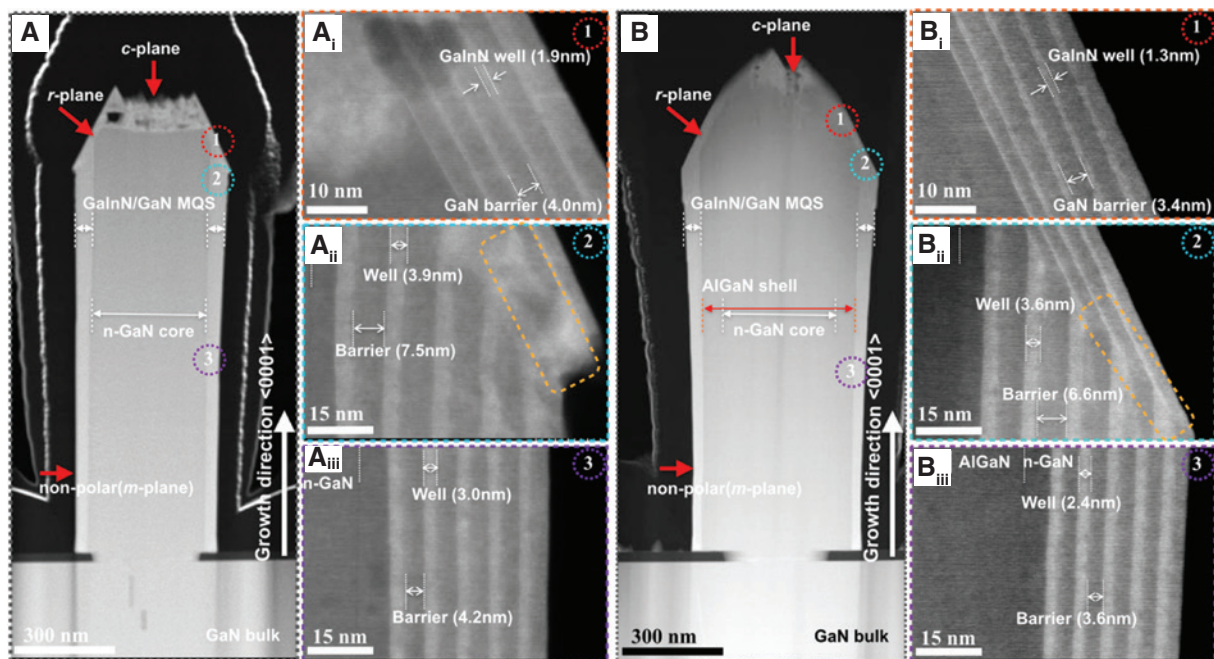


Figure 3: Cross-sectional STEM images of MQS NW samples b and d. (A) Low-magnification STEM image of sample b, taken along the growth direction $\langle 0001 \rangle$ (the diameter of n-core is 343 nm). The high-magnification HAADF STEM images of the MQS structures: (A_i) semipolar *r*-plane, (A_{ii}) near junction between *r*-plane and *m*-plane, and (A_{iii}) the middle area of the *m*-plane. The bright contrast corresponds to the GaInN, and the darker area to GaN. (B) Low-magnification STEM image of sample d (the diameter of n-core and AlGaIn undershell is 459 nm). The high-magnification HAADF STEM images of the MQS structures (B_i) on *r*-plane, (B_{ii}) near junction between *r*- and *m*-planes, and (B_{iii}) the middle area of the *m*-plane.

incorporated with Ga and homogeneously distributed over the surface area of the apex [35]. Ga droplets were speculated to form on the apex, resulting in a rough morphology. In addition, the STEM image of the apex part shows that some voids formed on the *c*-plane during MQS growth. The interfaces between barriers and wells are indistinguishable at the *c*-plane, because of the fast growth rate on the *c*-plane and additional migration of adatoms from the slow growth facets (*r*-planes). The MQSs on the *c*-plane exhibit no obvious interface between the MQS and n-core, as shown in Figure 4 (A_{iii}). Dislocation and pyramidal defects [36, 37] are clearly visible near the apex part on the *c*-plane, which exhibit a dark contrast without abrupt boundaries. The high resolution of the atomic contrast HAADF-STEM images of the *m*-plane MQS on the NW in Figure 4 (A_{iv}) and (A_v) show the lattice arrangement, confirming the single crystallinity of GaInN/GaN structures. In comparison to the apex part, the *m*-planes are free of dislocations except some point defects. The formation of voids and pyramidal defects on the *c*-plane were significantly suppressed by employing an AlGaIn undershell, as illustrated in Figure 4B. Higher crystalline quality was observed in Figure 4 (B_{iii}), in spite of the indistinguishable interface of AlGaIn/GaN owing to the low Al incorporation. Moreover, it can be confirmed that the GaInN/GaN structures on the top and bottom areas of *m*-planes are free of point defects and

dislocations, as shown in Figure 4 (B_{iv}) and (B_v). Hence, the AlGaIn shell indeed not only plays an important role in trapping the point defects diffusion from n-core to MQSs but also improves the grown crystalline quality on *c*-planes.

Since the growth conditions, template substrate, and configuration of the MOCVD reactor have critical impacts on the *c*-, *r*-, and *m*-planes MQS structures, it is difficult to theoretically estimate the In incorporation. A comprehensive study of optical features was performed by using macro- and micro-PL characterizations. The room temperature PL spectra measurements were carried out on the NW samples without MQS, illuminated by a 325-nm laser. Here, the samples were probed using the macro-PL setup as depicted in Figure 1A. The PL spectra are as shown in Figure 5A, and one can observe a strong yellow emission located at 565 nm. Compared with the emission from the commercial substrate, an enhanced emission intensity is observed in n-core NWs (sample a). The yellow emission in the n-core is ascribed to the point defects involved during high-temperature growth. By using an AlGaIn undershell, the signal of this yellow emission is suppressed, which verified the effect of the AlGaIn undershell on suppressing point defects. The PL spectra of as-grown MQS NW samples b and d were probed by macro-PL using a 405 nm laser as the excitation source. Figure 5B shows the results of the NW samples recorded at room temperature. The

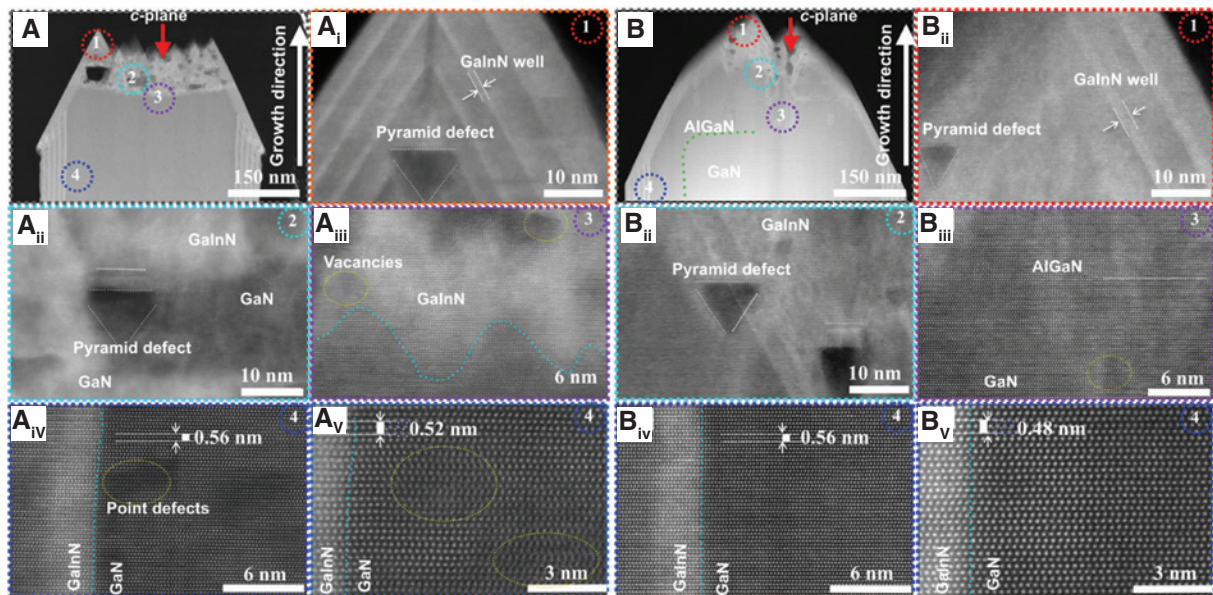


Figure 4: STEM images of the interface between the MQS and core structures at the apex part and *m*-planes in samples b and d. (A) Low-magnification STEM image of the top area of a NW in sample b. The higher magnification STEM images of the (A_i) apex structure grown on *c*-plane, (A_{ii}) the mixture MQS structure in *c*-plane, and (A_{iii}) the interface area between n-core and MQS structures in the *c*-plane. (A_{iv}) and (A_v) show the high-resolution atomic contrast STEM images of the interface between MQS and n-core of *m*-plane on the top and bottom areas of a NW in sample b. (B) Low-magnification STEM image of sample d. Higher magnification STEM images of the (B_i) apex structure, (B_{ii}) the mixture MQS structure on *c*-plane, and (B_{iii}) the interface area between the n-core and AlGaIn shell on the *c*-plane. (B_{iv}) and (B_v) show the high-resolution atomic contrast STEM images of the interfaces of the first pair well/barrier on *m*-planes at the top and bottom areas of a NW.

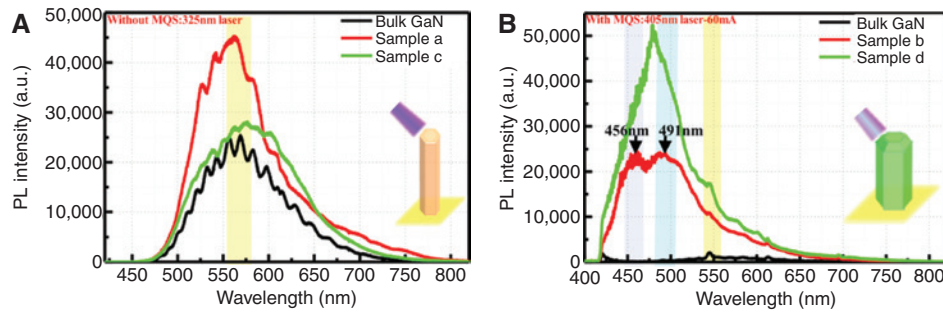


Figure 5: Macro-PL spectra of the NWs in samples a, b, c, and d.

(A) Macro-PL spectra of the bulk GaN and NW samples a and c, respectively, illuminated by a 325 nm laser. (B) Macro-PL spectra of NW samples b and d, which were measured by using 405 nm excitation wavelength.

broad emission peak located at 450–500 nm consists of the signal of MQS on the *c*-, *r*-, and *m*-planes from 750 NW arrays. The existence of two distinct peaks (456 nm and 491 nm) in sample b indicates the presence of different In concentrations on different regions of the NWs, mainly from the *m*- and *r*-planes. During the growth of MQS, the impinging rate of adatoms on the top area (*c*- and *r*-planes) is much higher than that of the *m*-plane sidewalls [38]. Thus, the longer emission peak at 490 nm is ascribed to the emission from *r*-planes, while the shorter one is from *m*-planes of NWs. The PL intensity is increased 2.3 times in sample d in comparison to that without the AlGaIn undershell. However, the dislocation defects are visible on the *c*-plane from the STEM results, where the emission is expected to be much weaker than that of *m*-planes. Therefore, the emissions from *r*- and *m*-planes are equivalently dominant contributions due to the configuration feature of the macro-PL setup with 45° incident angle. It should be noted that the 405 nm excitation wavelength is not suitable to excite the luminescence from the point defects in the *n*-core, which is mostly fed with a higher-energy excitation above the GaN band edge [39]. It is expected that the blue peak originates from the emission of the MQS on the *m*-planes, whereas the green peak arises from the In-rich region at the junction between the *m*- and the *r*-planes.

For a better understanding of the effects of AlGaIn undershell on optical properties, low temperature micro-PL measurements were performed for the NW samples. Figure 6A and B show the PL spectra of samples b and d, measured at room temperature and 12 K, respectively. It seems that the broad emission spectrum consists of three separated signals, i.e. the emissions from MQS on the *c*-, *r*-, and *m*-planes (75 NW arrays). Namely, the micro-PL emission spectrum is a result of merging three different peaks from different parts of the NWs. Therefore, the PL spectra can be fitted using three Gaussian components. It is believed that emission peak I is attributed to the MQS on *m*-planes while peak II is the resultant emission

from *r*-planes, and peak III originates from the GaInN layer on the apex part (small area). However, the dislocation defects and triangular defects determine the weaker emissions than that of *m*-planes. The internal quantum efficiency (IQE) value can be approximately derived by comparing PL intensity at room temperature with respect to that measured at low temperature [40]: $\text{IQE}(RT) = I(RT)/I(LT)$, where $I(RT)$ and $I(LT)$ denote the integrated intensity of PL measured at room temperature (300 K) and low temperature (12 K). Assuming the IQE at 12 K is 100%, the estimated IQE values for samples b and d are 29.32% and 35.52% at room temperature, respectively. The improved IQE in sample d is attributed to the unique AlGaIn undershell, which can suppress the point defects diffusion and reduce the MQS growth-induced dislocation densities on *c*-planes. In order to further investigate the progression of emission in NWs, excitation power-dependent PL measurements were performed on these samples, as shown in Figure 6C and D. Both samples exhibit a linear increase of integrated intensity as a function of excitation power. Theoretically, the electron-hole pair concentration in the quantum well increases with excitation power, which can screen the piezoelectric field and induce a blueshift of the emission peak on polar plane (QCSE) [41]. Since the emissions from *r*- and *m*-planes are dominant, no obvious blueshift of power-dependent PL is observed in these two NW samples.

To exclude the effects of measurement configuration of PL setups, the reflectance for the coaxial NW structures was numerically investigated by a three-dimensional finite difference time domain method. The simulation was carried out using rigorous coupled wave analysis method in the commercial RSoft Photonics CAD Suite software (Synopsys and RSoft Design Group, Synopsys Inc., Mountain View, CA, USA). A plane-wave excitation source from the topside of NWs was used for the reflectance simulation. The details of the simulation process can be found in a previous paper [13]. The reflectance for MQS NW arrays was simulated

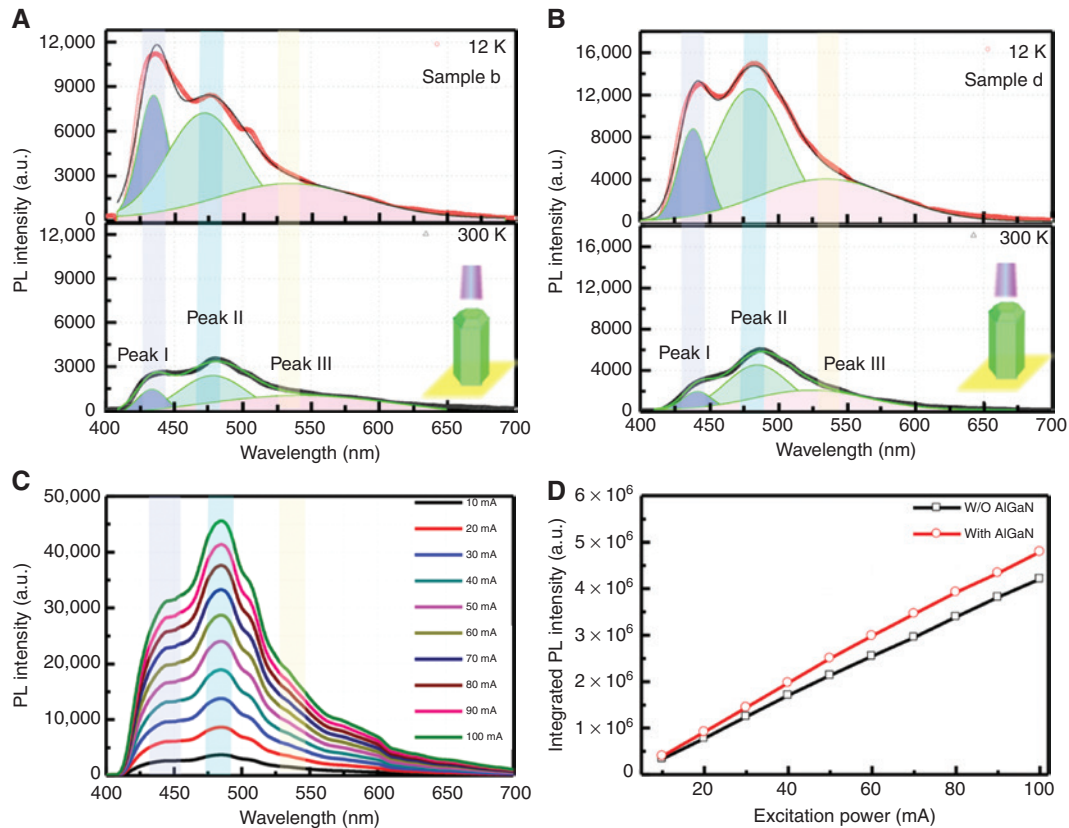


Figure 6: Low temperature and the power-dependent micro-PL spectra of the NW samples. Micro-PL spectra of the NW (A) sample b and (B) sample d, measured at 300 K and 12 K. (C) Power-dependent PL spectra of sample d. (D) The integrated PL intensity in samples b and d as a function of excitation power.

for the macro- and micro-PL setup, as well as the case in planar multiple-quantum wells (MQW) structures. The geometrical model for the NW samples was fitted according to the dimensions from SEM images in Figure 2. The results in Figure 7 reveal that the reflectance in NW MQS structures is lower than that of plain MQW over the simulated wavelength range, 400–800 nm. For the macro-PL

case in Figure 7A, the reflectance in NWs almost decreases linearly as wavelength increases. In Figure 7B, it is noted that the local minimum point of light reflectance redshifts towards longer wavelengths in NWs, due to the increase of the NW diameter with AlGaIn undershell. In both cases, the reflectance in NWs is comparable to that without an undershell. Therefore, it is believed that the observed PL

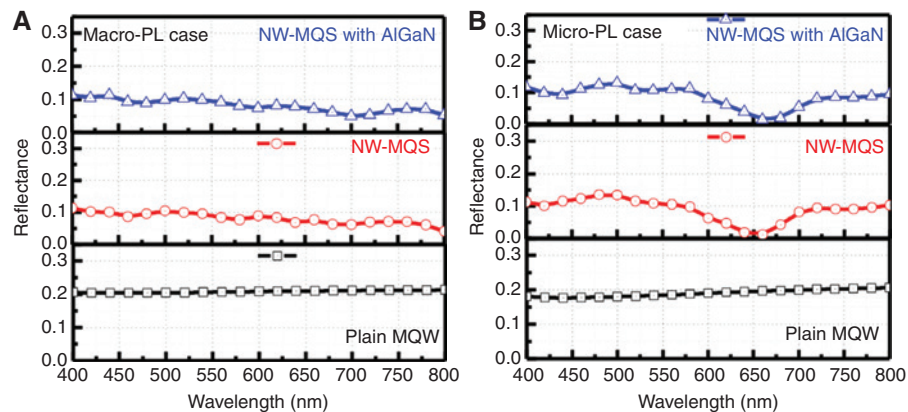


Figure 7: The three-dimensional simulation results of reflectance in NW samples. (A) Simulation of the reflectance in NW samples with 45° incident angle for macro-PL setup. (B) Calculated reflectance spectra in NWs, while the excitation and detection are perpendicular to the substrate (c-plane).

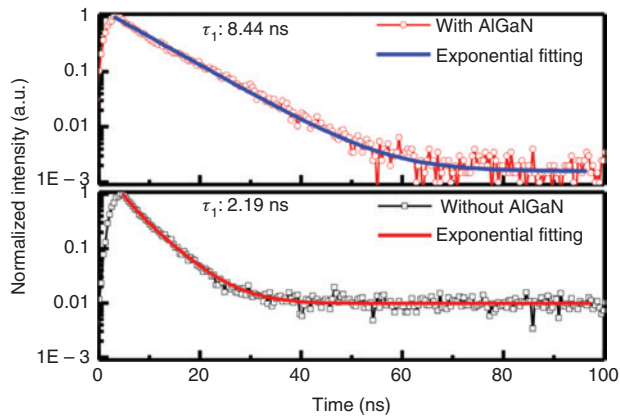


Figure 8: Time-resolved PL spectra of the NW samples b and d at room temperature, fitted with double-exponential decay function.

enhancement in NWs with an AlGaIn undershell is mainly attributed to the blocking of point defects diffusion.

The PL spectra reveal that In composition of the InGaIn/GaN MQW layer grown with the same conditions exhibits a slight difference in the *m*-plane and *r*-plane. In addition, the growth rate of the *r*-plane is much lower than that of the *c*-plane and *m*-plane, since the adatoms migration and In diffusion at the *r*-plane is slower than at the *m*-plane [42]. In addition to the temperature-dependent PL spectra, time-resolved PL measurements were performed to understand the effects of AlGaIn undershell. The decay curves from samples b and d are illustrated in Figure 8, fitted by a two-exponential model. The PL intensity as a function of time is described as follows [43]: $I(t) = A_1 \exp(-t/\tau_1) + A_2 \exp(-t/\tau_2)$, where τ_1 and τ_2 represent the fast and slow decay lifetimes and A_1 and A_2 are constants, respectively. The fast decay component τ_1 corresponds to both radiative and non-radiative recombination processes in GaInN/GaN MQS [44]. The fitted carrier lifetimes (fast component) for samples b and d are 2.19 ns and 8.44 ns, respectively. It was reported that point defects and impurities are the main factors determining emission intensity rather than threading dislocations [22, 23, 40]. Hence, it reveals that the emission intensity in MQS increases by employing the AlGaIn undershell, mainly due to the reduction of point defects density in the MQS active area including the *c*-, *r*-, and *m*-planes. It is speculated that the AlGaIn undershell reduces the point defects as well as dislocations in the *c*-plane, as confirmed via STEM results. Therefore, the enhancement of PL emission and IQE in sample d is mainly attributed to the effects of AlGaIn undershell. Nevertheless, the IQE is expected to be further increased by improving the spatial distribution of Al and In incorporation along the *m*-planes on sidewalls [38].

4 Conclusion

In conclusion, we gained an insight into the structural and optical properties of coaxial GaInN/GaN MQS NWs with an AlGaIn undershell. The structural and optical features of the core-shell NW structures have been addressed on three different facets (*c*-, *r*-, and *m*-planes). The structural properties of the NWs were investigated by HAADF-STEM imaging, indicating structural uniformity and free of dislocations inside the core structures. The In-rich droplets at the junction between *r*- and *m*-planes have been eliminated. The high resolution of HAADF-STEM clarified that the point defects diffusion from *n*-core to MQS region has been effectively suppressed on *m*-planes of NWs by employing an AlGaIn undershell. Moreover, the pyramidal defect and voids formation were significantly reduced on the apex region. Macro-PL measurements of NW samples proved the effective suppression of point defects by the AlGaIn undershell. The PL intensity of MQSs was increased 2.3 times in NW sample in comparison to that without the AlGaIn undershell. The time-resolved PL results clarified the superior quality of coaxial GaInN/GaN MQS NWs in terms of a significantly elongated carrier lifetime from 2.19 ns to 8.44 ns in NW samples before and after employing an AlGaIn undershell. The feasibility in obtaining low point defects and dislocation-free *m*-plane coaxial NWs using MOCVD can be utilized for the realization of high-performance white and micro-LEDs.

Acknowledgment: This work was financially supported by MEXT “Program for research and development of next-generation semiconductor to realize energy-saving society”, MEXT “Private University Research Branding Project”, JSPS KAKENHI for Scientific Research A [No. 15H02019], JSPS KAKENHI for Scientific Research A [No. 17H01055], JSPS KAKENHI for Innovative Areas [No. 16H06416], and Japan Science and Technology CREST [No. 16815710].

Author contributions: W.L. grew the NW samples, analyzed the results, and wrote the manuscript. M.T. did the simulation of light reflectance in NWs. D.H. measured the temperature-dependent, power-dependent PL spectra and time-resolved PL. N.S., N.G., and K.I. assisted with the MOCVD growth. D.H., T.T., and S.K. joined in the discussion and revised the manuscript. S.K., T.T., M.I., and I.A. contributed to the data analysis and supervised the project.

References

- [1] Akasaki I, Amano H. Crystal growth and conductivity control of group III nitride semiconductors and their application to short wavelength light emitters. *Jpn J Appl Phys* 1997;36:5393.
- [2] Akasaki I, Amano H. Breakthroughs in improving crystal quality of GaN and invention of the p–n junction blue-light-emitting diode. *Jpn J Appl Phys* 2006;45:9001.
- [3] Takeuchi T, Sota S, Katsuragawa M, et al. Quantum-confined Stark effect due to piezoelectric fields in GaInN strained quantum wells. *Jpn J Appl Phys* 1997;36:L382.
- [4] Takeuchi T, Wetzel C, Yamaguchi S, et al. Determination of piezoelectric fields in strained GaInN quantum wells using the quantum-confined Stark effect. *Appl Phys Lett* 1998;73:1691–3.
- [5] Kuykendall TR, Schwartzberg AM, Aloni S. Gallium nitride nanowires and heterostructures: toward color-tunable and white-light sources. *Adv Mater* 2015;27:5805–12.
- [6] Nguyen HP, Cui K, Zhang S, et al. Controlling electron overflow in phosphor-free InGaIn/GaN nanowire white light-emitting diodes. *Nano Lett* 2012;12:1317–23.
- [7] Hong Y, Lee CH, Yoon A, et al. Visible-color-tunable light-emitting diodes. *Adv Mater* 2011;23:3284–8.
- [8] Tchernycheva M, Lavenus P, Zhang H, et al. InGaIn/GaN core-shell single nanowire light emitting diodes with graphene-based P-contact. *Nano Lett* 2014;14:2456–65.
- [9] Qian F, Li Y, Gradecak S, et al. Multi-quantum-well nanowire heterostructures for wavelength-controlled lasers. *Nat Mater* 2008;7:701–6.
- [10] Nami M, Stricklin IE, DaVico KM, et al. Carrier dynamics and electro-optical characterization of high-performance GaN/InGaIn core-shell nanowire light-emitting diodes. *Sci Rep* 2018;8:501.
- [11] Monavian M, Rashidi A, Feezell D. A decade of nonpolar and semipolar III-nitrides: a review of successes and challenges. *Phys Status Solidi A* 2018;1800628.
- [12] Li C, Wright JB, Liu S, et al. Nonpolar InGaIn/GaN core-shell single nanowire lasers. *Nano Lett* 2017;17:1049–55.
- [13] Terazawa M, Ohya M, Iida K, et al. Hybrid simulation of light extraction efficiency in multi-quantum-shell (MQS) NW (nanowire) LED with a current diffusion layer. *Jpn J Appl Phys* 2019;58:SCCC17.
- [14] Li S, Waag A. GaN based nanorods for solid state lighting. *J Appl Phys* 2012;111:071101.
- [15] Liao CH, Chang WM, Chen HS, et al. Geometry and composition comparisons between c-plane disc-like and m-plane core-shell InGaIn/GaN quantum wells in a nitride nanorod. *Opt Express* 2012;20:15859–71.
- [16] Sekiguchi H, Kishino K, Kikuchi A. Emission color control from blue to red with nanocolumn diameter of InGaIn/GaN nanocolumn arrays grown on same substrate. *Appl Phys Lett* 2010;96:231104.
- [17] Li Q, Wang GT. Spatial distribution of defect luminescence in GaN nanowires. *Nano Lett* 2010;10:1554–8.
- [18] Armstrong A, Li Q, Bogart KHA, Lin Y, Wang GT, Talin AA. Deep level optical spectroscopy of GaN nanorods. *J Appl Phys* 2009;106:053712.
- [19] Carter DJ, Fuchs M, Stampfl C. Vacancies in GaN bulk and nanowires: effect of self-interaction corrections. *J Phys Condens Matter* 2012;24:255801.
- [20] Obata T, Iwata JI, Shiraishi K, Oshiyama A. First principles studies on In-related nitride semiconductors. *J Cryst Growth* 2009;311:2772–5.
- [21] Faleev N, Jampana B, Jani O, et al. Correlation of crystalline defects with photoluminescence of InGaIn layers. *Appl Phys Lett* 2009;95:051915.
- [22] Schubert MF, Chhajed S, Kim JK, et al. Effect of dislocation density on efficiency droop in GaInN/GaN light-emitting diodes. *Appl Phys Lett* 2007;91:231114.
- [23] Shabunina E, Averkiev N, Chernyakov A, Levinshtein M, Petrov P, Shmidt N. Extended defect system as a main source of non-radiative recombination in InGaIn/GaN LEDs. *Phys Status Solidi (C)* 2013;10:335–7.
- [24] Robin Y, Bae SY, Shubina TV, et al. Insight into the performance of multi-color InGaIn/GaN nanorod light emitting diodes. *Sci Rep* 2018;8:7311.
- [25] Kapoor A, Guan N, Vallo M, et al. Green electroluminescence from radial m-plane InGaIn quantum wells grown on GaN wire sidewalls by metal–organic vapor phase epitaxy. *ACS Photonics* 2018;5:4330–7.
- [26] Lin YT, Yeh TW, Nakajima Y, Dapkus PD. Catalyst-free GaN nanorods synthesized by selective area growth. *Adv Funct Mater* 2014;24:3162–71.
- [27] Boubanga-Tombet S, Wright JB, Lu P, et al. Ultrafast carrier capture and Auger recombination in single GaN/InGaIn multiple quantum well nanowires. *ACS Photonics* 2016;3:2237–42.
- [28] Bae SY, Jung BO, Lekhal K, et al. Structural and optical study of core-shell InGaIn layers of nanorod arrays with multiple stacks of InGaIn/GaN superlattices for absorption of longer solar spectrum. *Jpn J Appl Phys* 2016;55:05FG03.
- [29] Armstrong A, Li Q, Lin Y, Talin AA, Wang GT. GaN nanowire surface state observed using deep level optical spectroscopy. *Appl Phys Lett* 2010;96:163106.
- [30] Albrecht M, Lymperakis L, Neugebauer J, et al. Chemically ordered Al_xGa_{1-x}N alloys: spontaneous formation of natural quantum wells. *Phys Rev B* 2005;71:035314.
- [31] Warnick KH, Puzyrev Y, Roy T, Fleetwood DM, Schrimpf RD, Pantelides ST. Room-temperature diffusive phenomena in semiconductors: the case of AlGaIn. *Phys Rev B* 2011;84:214109.
- [32] Henry TA, Armstrong A, Allerman AA, Crawford MH. The influence of Al composition on point defect incorporation in AlGaIn. *Appl Phys Lett* 2012;100:043509.
- [33] Chichibu S, Uedono A, Kojima K, et al. The origins and properties of intrinsic nonradiative recombination centers in wide bandgap GaN and AlGaIn. *J Appl Phys* 2018;123:161413.
- [34] Pennycook S, Boatner L. Chemically sensitive structure-imaging with a scanning transmission electron microscope. *Nature* 1988;336:565.
- [35] Park JH, Chatterjee U, Kang S, Lee K, Kim JS, Lee CR. Synthesis of hybrid nanowires comprising uniaxial and coaxial InGaIn/GaN MQWs with a nano-cap. *J Mater Chem C* 2016;4:10005–10.
- [36] Vennéguès P, Benaissa M, Beaumont B, et al. Pyramidal defects in metalorganic vapor phase epitaxial Mg doped GaN. *Appl Phys Lett* 2000;77:880–2.
- [37] Iwata K, Narita T, Nagao M, et al. Atomic resolution structural analysis of magnesium segregation at a pyramidal inversion domain in a GaN epitaxial layer. *Appl Phys Express* 2019;12:031004.
- [38] Lu W, Sone N, Goto N, et al. Effect of AlGaIn undershell on the cathodoluminescence properties of coaxial GaInN/GaN multiple-quantum-shells nanowires. *Nanoscale* 2019;11:18746–54.
- [39] Wang X, Li S, Fündling S, et al. Polarity control in 3D GaIn structures grown by selective area MOVPE. *Cryst Growth Des* 2012;12:2552–6.

- [40] You G, Liu J, Jiang Z, et al. Enhanced radiative recombination and suppressed Auger process in semipolar and nonpolar InGaIn/GaN quantum wells grown over GaN nanowires. *Opt Lett* 2014;39:1501–4.
- [41] Koester R, Hwang JS, Salomon D, et al. M-plane core-shell InGaIn/GaN multiple-quantum-wells on GaN wires for electroluminescent devices. *Nano Lett* 2011;11:4839–45.
- [42] Ra YH, Navamathavan R, Park JH, Lee CR. Coaxial In(x)Ga(1-x)N/GaN multiple quantum well nanowire arrays on Si(111) substrate for high-performance light-emitting diodes. *Nano Lett* 2013;13:3506–16.
- [43] Liu B, Smith R, Athanasiou M, Yu X, Bai J, Wang T. Temporally and spatially resolved photoluminescence investigation of (1120305;2) semi-polar InGaIn/GaN multiple quantum wells grown on nanorod templates. *Appl Phys Lett* 2014;105:261103.
- [44] Zhang G, Guo X, Ren FF, et al. High-brightness polarized green InGaIn/GaN light-emitting diode structure with Al-coated p-GaN grating. *ACS Photonics* 2016;3:1912–8.